

# Mechanistic Study of the Li–Air Battery with a $\text{Co}_3\text{O}_4$ Cathode and Dimethyl Sulfoxide Electrolyte

Zhen Jiang and Andrew M. Rappe\*



Cite This: *J. Phys. Chem. C* 2021, 125, 21873–21881



Read Online

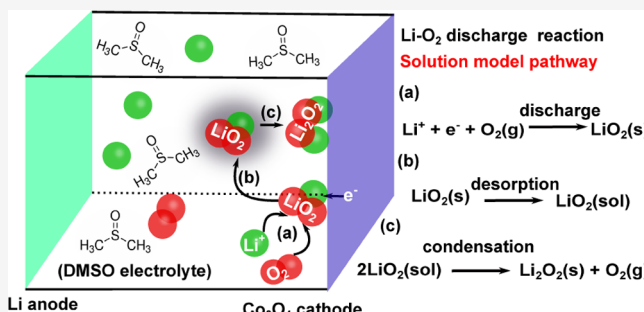
ACCESS |

Metrics & More

Article Recommendations

Supporting Information

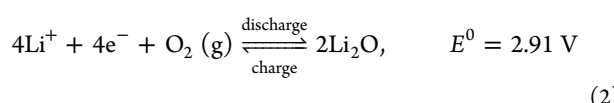
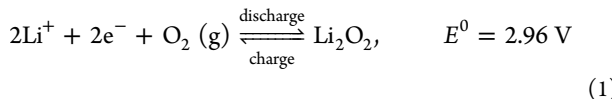
**ABSTRACT:** The lithium–air battery, a powerful competitor to replace the traditional lithium-ion battery, has attracted increasing attention due to its extremely high theoretical energy density. However, its development is limited by the cathode and electrolyte properties, which should include high stability, conductivity, and electrocatalytic properties in oxygen-rich environments. Here, we employ a systematic first-principles study of  $\text{Li}–\text{O}_2$  discharge and charge reactions on the  $\text{Co}_3\text{O}_4$ -based cathode with the assistance of dimethyl sulfoxide (DMSO) electrolyte. The structure, stability, and electronic properties of different surface reconstructions of the  $\text{Co}_3\text{O}_4(100)$  facet are investigated. In addition, the mechanisms and thermodynamic overpotentials of multi-step reactions between  $\text{Li}^+/\text{e}^-$  and  $\text{O}_2$  are provided, where lithium suboxide products ( $\text{Li}_2\text{O}_2$  or  $\text{Li}_3\text{O}_2$ ) are formed on the different  $\text{Co}_3\text{O}_4(100)$  terminations. The solvation shell of  $\text{Li}^+$  components in explicit DMSO solvent is investigated through *ab initio* molecular dynamics simulations. In general, we find that the  $\text{Co}_3\text{O}_4(100)\text{-O}$  (oxidized) surface is the most stable one under standard conditions, and the stable  $\text{Li}^+$  solvation structure is found in a tetrahedral  $\text{Li}(\text{DMSO})_4^+$  shell in the DMSO-based electrolyte. Moreover, in the system of the  $\text{Co}_3\text{O}_4(100)\text{-O}$  cathode and DMSO electrolyte, the solution model pathway is energetically favorable for the  $\text{Li}–\text{O}_2$  discharge reaction. It provides a low constant overpotential of 0.17 V during a long-term discharging process, thus causing the final toroid  $\text{Li}_2\text{O}_2$  formation on the cathode. During the charging process, an overpotential of 0.36 V is required to rapidly decompose  $\text{Li}_2\text{O}_2$ .



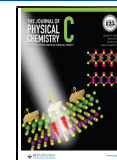
Although the  $\text{Li}_2\text{O}$  discharge product in [reaction 2](#) delivers higher energy density, breaking the O–O bond makes this reaction slow and possibly irreversible. Therefore, most of the current cathodes can only provide  $\text{Li}_2\text{O}_2$  as a product following [reaction 1](#).<sup>15,16</sup> To date,  $\text{Co}_3\text{O}_4$  is one of the most popular cathodes among metal oxides for Li–air batteries because it is active, conductive, and stable in an  $\text{O}_2$ -rich environment.<sup>17–19</sup> Moreover, according to the experimental reports, it can provide a low discharge overpotential during operation.<sup>20</sup> However, the mechanism of charge and discharge reactions on the  $\text{Co}_3\text{O}_4$  cathode is still unknown. Therefore, it is important to provide a systematic first-principles study of the roles of the  $\text{Co}_3\text{O}_4$  cathode toward  $\text{Li}–\text{O}_2$  reactions.

## INTRODUCTION

Recently, the great commercial value and environmental friendly properties of battery electric vehicles (BEVs) have attracted the attention of many companies. However, the development is limited by the energy storage technology.<sup>1–4</sup> The current rechargeable batteries are based on Li-ion batteries (LIBs), which offer a useable energy of up to 120 W·h/kg. In order to give a car a range of 200–300 miles, an ideal energy capacity of  $\approx$ 75 kW·h is required on a single charge.<sup>5–7</sup> Based on this, a very heavy battery (625 kg) is required in the vehicle, which will reduce its energy efficiency. Therefore, it is compelling to search for other battery designs to improve BEVs. Among many candidates, the Li–air battery is a promising energy storage paradigm, which can theoretically provide a specific energy of nearly 12.0 kW·h/kg (100 times the capacity of LIBs).<sup>8–11</sup> However, the current Li–air batteries can only provide a practical energy of 1.7 kW·h/kg, which is limited by many factors including cathode materials. Therefore, more systematic studies of Li–air batteries are needed. The overall discharge and charge reactions of the Li–air battery are<sup>12–14</sup>



Received: August 29, 2021  
 Revised: September 14, 2021  
 Published: October 5, 2021



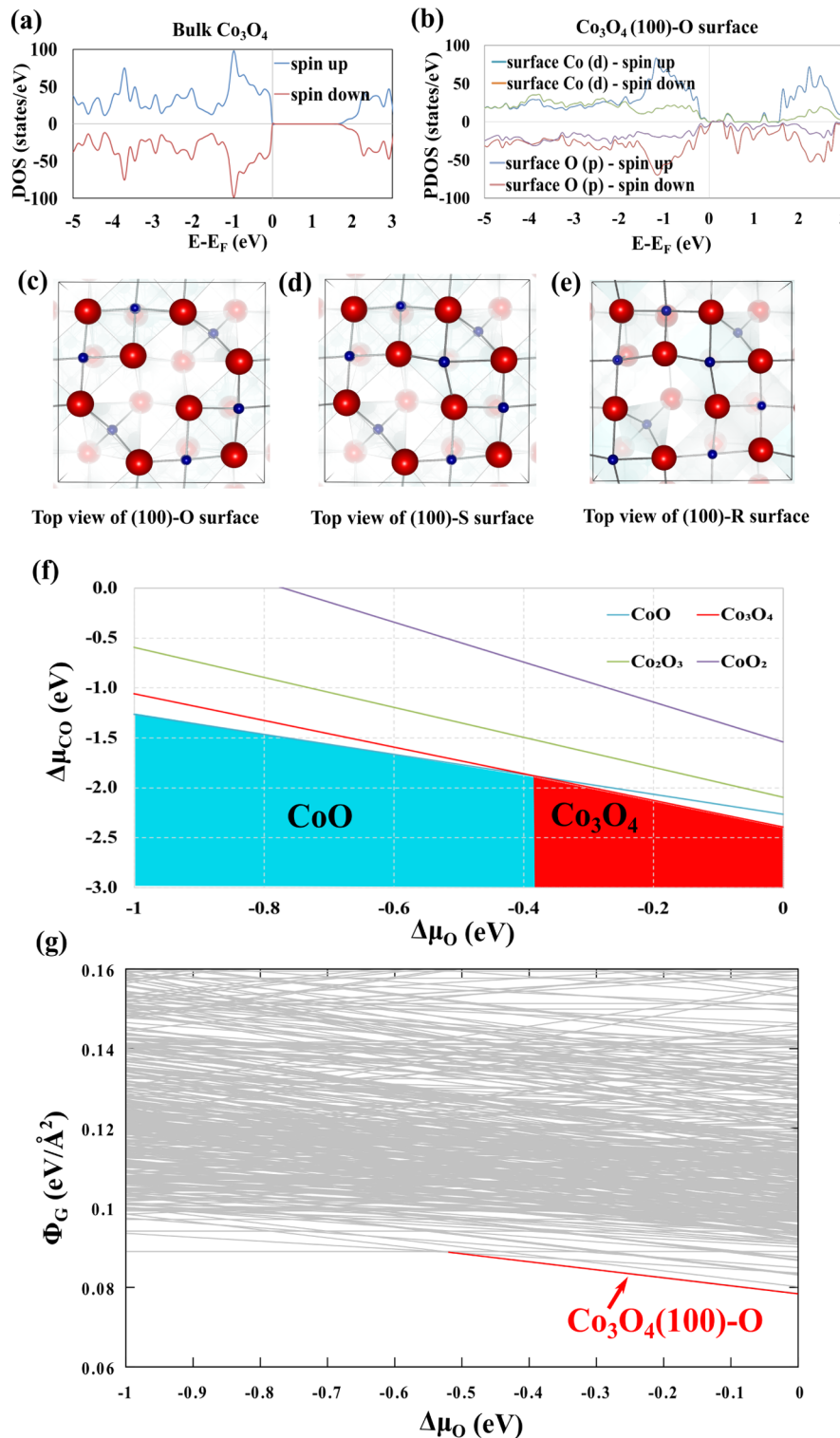


**Figure 1.** (a) Density of states (DOS) of bulk Co<sub>3</sub>O<sub>4</sub> and (b) projected DOS of the Co<sub>3</sub>O<sub>4</sub>(100)-O surface. (c–e) Top view of the Co<sub>3</sub>O<sub>4</sub>(100)-O, -S, and -R surfaces. (f) Phase diagram of bulk CoO, Co<sub>3</sub>O<sub>4</sub>, Co<sub>2</sub>O<sub>3</sub>, and CoO<sub>2</sub>. (g) Surface energy diagram of 500 reconstructed terminations of Co<sub>3</sub>O<sub>4</sub>(100) obtained from ai-GCMC.

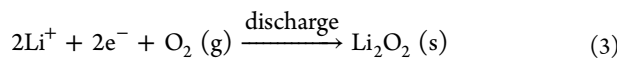
The structure and stability of Co<sub>3</sub>O<sub>4</sub> have been studied experimentally and theoretically.<sup>18,21,22</sup> Co<sub>3</sub>O<sub>4</sub> is an anti-ferromagnetic spinel oxide, including tetrahedrally coordinated Co<sup>2+</sup> (magnetic moment = 3.0  $\mu_B$  in the experiment and 2.69  $\mu_B$  in density functional theory, DFT) and octahedrally coordinated Co<sup>3+</sup> (0  $\mu_B$ ) ions.<sup>22</sup> The (100), (110), and (111) surfaces are the most prevalent facets exposed on Co<sub>3</sub>O<sub>4</sub>

based on previous observations.<sup>23,24</sup> Among these, the (100) facet has been confirmed to be the most stable by DFT calculations and is considered to be the main/only facet in many sustainable catalytic processes.<sup>22,25</sup> However, even for the (100) surface, there are three different symmetric pristine terminations, which are usually named (100)-O (oxidized), (100)-S (stoichiometric), and (100)-R (reduced) surfaces

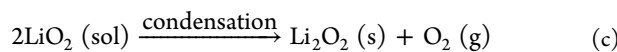
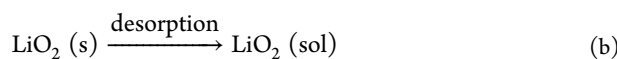
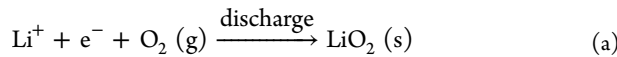
depending on the surface Co/O ratio (see Figure 1c–e). It was reported that the (100)-O surface is the most stable one under standard conditions ( $T^0 = 298.15\text{ K}$  and  $P_{\text{O}_2}^0 = 0.21\text{ atm}$ ).<sup>22,25</sup> However, the surface reconstruction behavior of the (100)-O facet, such as O or Co vacancy formation, has not been studied extensively. In addition, the electronic properties of these three surfaces have not been examined. Therefore, it is important to investigate the surface stability, properties, and reconstructions of a  $\text{Co}_3\text{O}_4(100)$  slab systematically before simulating the Li– $\text{O}_2$  reactions on it.

The mechanism and product growth pathways for the Li– $\text{O}_2$  discharge and charge reactions on  $\text{Co}_3\text{O}_4$  are still unknown. The superiority of  $\text{Co}_3\text{O}_4$  as a cathode relative to other transition metal oxides is due to low discharge and charge overpotentials ( $\eta_{\text{discharge}} \approx 0.1\text{--}0.3\text{ V}$ ,  $\eta_{\text{charge}} \approx 1\text{ V}$ ) reported experimentally.<sup>16,20</sup> However, the current  $\text{Co}_3\text{O}_4$ -based batteries still must be improved in both discharge and charge processes. Therefore, a systematic *ab initio* study is necessary to unveil the potential- and rate-determining steps for the multiple electron transfer steps in the overall Li– $\text{O}_2$  reactions. It is also notable that most theoretical calculations simulated the thin-film growth of the  $\text{Li}_2\text{O}_2$  discharge product on the cathodes, which should reduce catalytic activity from that of  $\text{Co}_3\text{O}_4$  to that of  $\text{Li}_2\text{O}_2(s)$ . However, this surface deactivation phenomenon is often ignored.<sup>26–29</sup> Indeed, on some recently proposed Li–air battery electrodes, toroid-shaped  $\text{Li}_2\text{O}_2$  nanoparticles were found after discharge (not blocking the electrode active sites).<sup>10,30,31</sup> The morphology change from thin film to toroid shape is attributed to the use of different electrolytes, thus indicating two different  $\text{Li}_2\text{O}_2$  growth pathways: the surface and solution models.<sup>32,33</sup>

#### Surface model



#### Solution model



In the surface model, all Li– $\text{O}_2$  reactions are completed on the cathode surface, resulting in thin-film discharge products. Regarding the solution model, the soluble  $\text{LiO}_2$  intermediates form *via* a and then desorb from the cathode surface into the electrolyte (b), followed by disproportionation of two  $\text{LiO}_2$  into insoluble  $\text{Li}_2\text{O}_2$  on the cathode surface (a toroid-shaped particle) (c). The discrimination between the two growth models is mainly influenced by the  $\text{LiO}_2$  desorption ability at the interface, which is closely determined from the donor number (*i.e.*, Lewis basicity) of the electrolyte.<sup>32,33</sup> The donor number is a representative parameter to indicate the ability of a solvent to solvate cations and small molecules by donating an electron pair, where a higher donor number relates to higher solubility. Recently, the solution model has become more important than the surface model in Li–air batteries because it can continuously provide a clean catalytic surface for the discharge reactions, yielding a low and constant discharge overpotential for a long time. Dimethyl sulfoxide (DMSO) is nearly always employed as the supporting electrolyte in recent

designs of Li–air batteries to facilitate the solution model discharge pathway.<sup>10,33,34</sup> Therefore, we investigate the roles of  $\text{Co}_3\text{O}_4$  facets and DMSO electrolyte toward Li– $\text{O}_2$  reactions from a first-principles DFT perspective. In this paper, we present a systematic first-principles study of the stability and reconstruction of  $\text{Co}_3\text{O}_4(100)$  facets, Li– $\text{O}_2$  reaction mechanisms and overpotentials, solvation structures of Li salts ( $\text{LiClO}_4$ ) in DMSO, the Li desolvation process at the  $\text{Co}_3\text{O}_4$ /DMSO interface, and pathways for discharge product growth on the  $\text{Co}_3\text{O}_4$  cathodes.

## RESULTS AND DISCUSSION

**Bulk  $\text{Co}_3\text{O}_4$ .** The optimized lattice parameter of cubic  $\text{Co}_3\text{O}_4$  is  $8.18\text{ \AA}$ , in agreement with previous DFT and experimental studies (Figure S1a).<sup>22,25</sup> The ground state of  $\text{Co}_3\text{O}_4$  is antiferromagnetic, where the magnetic moment of the octahedrally coordinated  $\text{Co}^{3+}$  is  $0\text{ }\mu_{\text{B}}$ , while the magnetic moment of the tetrahedrally coordinated  $\text{Co}^{2+}$  is  $2.65\text{ }\mu_{\text{B}}$ . The calculated electronic structure of bulk  $\text{Co}_3\text{O}_4$  shows it to be a semiconductor with a band gap of  $1.75\text{ eV}$  (Figure 1a), which is comparable with the previous experimental and theoretical values  $\approx 1.6\text{--}1.7\text{ eV}$ .<sup>22,25</sup>

**$\text{Co}_3\text{O}_4(100)$  Surface.** We start the simulation from three high-symmetry terminations, the  $\text{Co}_3\text{O}_4(100)\text{-O}$ , (100)-S, and (100)-R surfaces (Figure S1b). The optimized surface configurations are shown in Figure 1c–e, while the surface energies can be found in Table 1. We found that the

**Table 1. Surface Energy and Surface Band Gap of  $\text{Co}_3\text{O}_4(100)\text{-O}$ , -S, and -R Slabs**

surfaces	$\Phi_G$ (J/m <sup>2</sup> )	band gap (eV)
(100)-O	1.26	0.20
(100)-S	1.48	0.30
(100)-R	1.61	0

$\text{Co}_3\text{O}_4(100)\text{-O}$  surface is the most stable one with the lowest surface energy at  $T^0 = 298.15\text{ K}$  and  $P_{\text{O}_2}^0 = 0.21\text{ atm}$  and all conditions under which bulk  $\text{Co}_3\text{O}_4$  is stable. As shown in Figure 1c, the top layer is filled with octahedral  $\text{Co}^{3+}$  with one dangling bond, resulting in a pronounced change in the magnetic moment from  $0$  to  $2.0\text{ }\mu_{\text{B}}$ . As for the (100)-S or (100)-R surfaces, one or two tetrahedral Co atoms are initially added (per unit cell) on the top layer of the (100)-O surface (see Figure S1b). After optimization, the tetrahedral Co atoms are shifted to the square surface site formed by four adjacent O atoms, while the magnetic moment remains large,  $2.6\text{ }\mu_{\text{B}}$ . In addition, according to the electronic structure of the three terminations, the (100)-O and (100)-S facet remains a semiconductor, but the surface bands have a small band gap of  $0.2$  (Figure 1b) and  $0.3\text{ eV}$ , respectively (Table 1). For (100)-R surfaces, the surface is metallic.

Next, we consider more reconstruction possibilities of the  $\text{Co}_3\text{O}_4(100)$  surface by using the *ai*-GCMC method.<sup>35</sup> Co and O atoms will be moved, inserted, or deleted from the surface during the simulation. We start from the  $\text{Co}_3\text{O}_4(100)\text{-O}$  surface, which is determined as the most stable high-symmetry surface (see previous paragraph). The surface energy (grand potential  $\Phi_G|T=0$ , equation in Supporting Information) of all configurations obtained from the *ai*-GCMC simulation is plotted in Figure 1g as a function of  $\Delta\mu_{\text{O}}$ . We find that the  $\text{Co}_3\text{O}_4(100)\text{-O}$  surface is still the most stable one in a range of

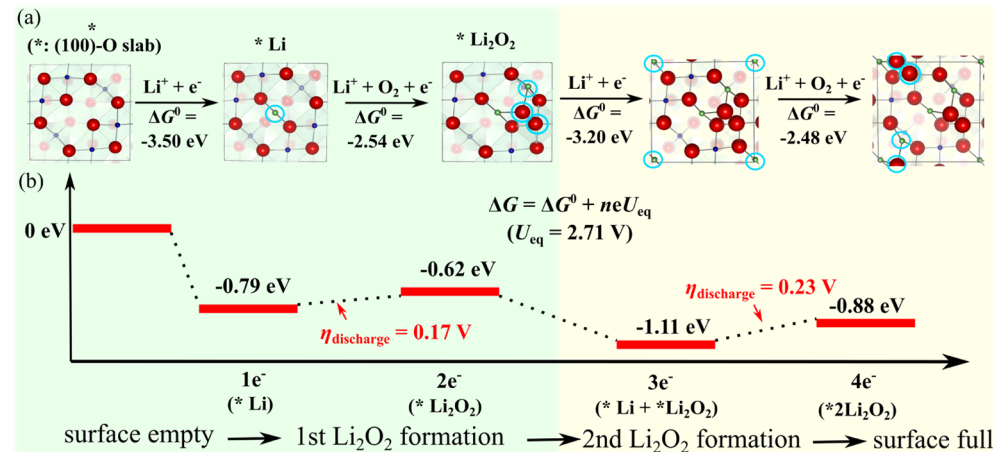


**Figure 2.** (a) Most thermodynamically favorable formation mechanisms of  $\text{Li}_2\text{O}_2$  monomers on the  $\text{Co}_3\text{O}_4(100)$ -O surface. \* denotes an adsorption site, and pre-pended \* denotes an adsorbed species, for example,  $^*\text{Li}$ . During each step, the newly adsorbed Li and  $\text{O}_2$  are circled in sky blue. (b) Free-energy diagram of  $\text{Li}^+/\text{e}^-$  and  $\text{O}_2$  reactions on the  $\text{Co}_3\text{O}_4(100)$ -O surface at the ideal equilibrium potential  $U_{\text{eq}} = 2.71 \text{ V}$ , where the  $\eta_{\text{discharge}}$  for the formation of first and second  $^*\text{Li}_2\text{O}_2$  (per surface cell) is shown.

$\Delta\mu_{\text{O}} = -0.5\text{--}0 \text{ eV}$ , covering the  $\Delta\mu_{\text{O}}$  range for bulk  $\text{Co}_3\text{O}_4$  stability ( $\Delta\mu_{\text{O}} = -0.38\text{--}0 \text{ eV}$ , Figure 1f). All the reconstructed surfaces, including those formed by adding more Co/O atoms or making Co/O vacancies, are found to be unfavorable. Therefore, we can conclude that the  $\text{Co}_3\text{O}_4(100)$ -O surface is the predominant facet for  $\text{Co}_3\text{O}_4$  particles. In addition, when the  $\Delta\mu_{\text{O}}$  was decreased beyond the bulk stability region, the  $\text{Co}_3\text{O}_4(100)$ -S and -R surfaces are stable (despite bulk metastability), which is in agreement with previous DFT reports.<sup>25,36,37</sup> Therefore, we systematically studied the catalytic activity of the  $\text{Co}_3\text{O}_4(100)$ -O facet for  $\text{Li}-\text{O}_2$  reactions (see below sections), while the catalytic performance of  $\text{Co}_3\text{O}_4(100)$ -S, and -R surfaces can be found in Supporting Information.

**Thermodynamic Overpotential Study of  $\text{Li}-\text{O}_2$  Reactions on the  $\text{Co}_3\text{O}_4(100)$ -O Surface.** Figure 2 shows the most favorable mechanistic and thermodynamic performance for the discharge reaction between  $\text{Li}^+/\text{e}^-$  and  $\text{O}_2$  on the  $\text{Co}_3\text{O}_4(100)$ -O surface. The effect of DMSO solvent can be ignored when we calculate the theoretical overpotentials in Figure 2, based on the computational model of the lithium electrode provided by Nørskov's group.<sup>38</sup> Because the solvation reactions are not redox reactions, the electrolyte contribution affects the barriers of interfacial adsorption/desorption reactions through the pre-factor of the rate expression (kinetic calculations) but not the potential-dependent thermodynamics in this study.<sup>38</sup> In addition, the DFT-defined reference free energy of  $\text{Li}^+/\text{e}^-$  (transfer components during charging and discharging) is computed from the bulk Li metal (anode material) in this method,<sup>38–40</sup> while lithium ions in solution are assumed to be in equilibrium with the lithium metal anode and with  $\text{Li}^+$  near the cathode surface.<sup>38</sup> Therefore, the solvation effect on the calculations of the  $\text{Li}^+/\text{e}^-$  transfer reaction is quite small and can be ignored in the estimation of overall discharging/charging reactions between the Li anode and cathode surface.<sup>38</sup> Using this model, we derived DFT-level overpotentials as shown in Figure 2. The same method has been well-tested by many theorists on other electrode materials, obtaining very good estimates of DFT-level overpotentials compared with those of experiments.<sup>10,29,39–41</sup> Therefore, our DFT-derived overpotentials (in Figure 2) can

be directly compared with other computationally estimated overpotentials on various materials in this Li-air battery field.

As shown in Figure 2, the initial  $\text{Li}^+/\text{e}^-$  adsorption is extremely exothermic, with  $\Delta G^0 = -3.50 \text{ eV}$ . The Li cation will be adsorbed at a bridge site equidistant between two surface O anions, where there is no tetrahedral Co ion directly below in the top subsurface layer. Then, the second pair of  $\text{Li}^+/\text{e}^-$  will be transferred to the neighboring O–O bridge site (right above the subsurface tetrahedral Co), while  $\text{O}_2$  is bonded to the adjacent Co atom on the surface, eliminating the dangling bond of a surface Co (by forming a new Co–O bond). By this mechanism, the first  $^*\text{Li}_2\text{O}_2$  is formed. Another less favorable mechanism to form one  $^*\text{Li}_2\text{O}_2$  can be found in Figure S2, which is also based on the  $^*\text{Li}$  intermediate. We also considered the pathways based on the  $^*\text{LiO}_2$  intermediate (assumed in many experiments). However, for this cathode, we found that the Gibbs free energy ( $\Delta G^0 = -3.50 \text{ eV}$ ) of  $^*\text{Li}$  formation is more favorable than that ( $\Delta G^0 = -2.99 \text{ eV}$ ) of  $^*\text{LiO}_2$  formation after the first electron transfer step. In addition, we also find that the free energy of the  $\text{O}_2$  adsorption reaction ( $^*\text{Li}(\text{s}) + \text{O}_2(\text{g}) \rightarrow ^*\text{LiO}_2$ ) is  $\Delta G^0 = 0.51 \text{ eV}$ , while the Gibbs free energy of  $^*\text{Li}(\text{s}) + \text{Li}^+ + \text{e}^- \rightarrow ^*\text{2Li}(\text{s})$  is  $\Delta G^0 = -0.20 \text{ eV}$  (at  $U_{\text{eq}} = 2.71 \text{ V}$ ). Therefore, we know that the second  $^*\text{Li}$  formation will proceed before the adsorption of  $\text{O}_2$ , avoiding the existence of the  $^*\text{LiO}_2$  intermediate on the  $\text{Co}_3\text{O}_4(100)$ -O surface. The same pathway (without  $^*\text{LiO}_2$  intermediate formation) has also been found for  $\text{Li}-\text{O}_2$  reactions on the  $\text{CeO}_2$  surface in another study.<sup>41</sup> After the first monomer formation, the remaining half of the active sites (Co and O–O bridge sites) on the  $\text{Co}_3\text{O}_4(100)$ -O surface can provide an energetically favorable pathway to form the second  $^*\text{Li}_2\text{O}_2$  (per surface cell) with the same mechanism of the first  $^*\text{Li}_2\text{O}_2$ . The formation of the second  $^*\text{Li}_2\text{O}_2$  is a bit less exothermic due to the steric hindrance from the first  $^*\text{Li}_2\text{O}_2$ . After the second  $^*\text{Li}_2\text{O}_2$  formation, the surface (of our simulation model,  $8.18 \times 8.18 \text{ \AA}^2$ ) is fully covered with  $\text{Li}_2\text{O}_2(\text{s})$ , and there are no active O–O bridge sites left for additional  $\text{Li}^+$  adsorption. The free-energy diagram for  $\text{Li}-\text{O}_2$  reactions on the  $\text{Co}_3\text{O}_4(100)$ -O surface is plotted at the ideal equilibrium potential  $U_{\text{eq}} = 2.71 \text{ V}$  (Figure 2b). As shown, the discharge potential-determining step is the second step ( $^*\text{Li} + \text{Li}^+ + \text{e}^- + \text{O}_2 \rightarrow ^*\text{Li}_2\text{O}_2$ ) with overpotentials (making

all steps downhill) of 0.17 V and 0.23 V for the formation of both first and second  $*\text{Li}_2\text{O}_2$ , respectively.

### Effect of DMSO Solvent Toward the Li–O<sub>2</sub> Reactions.

Here, we consider the solvation effects of DMSO toward the configurations in Figure 2a. The first step is to obtain the structural properties of Li<sup>+</sup> and O<sub>2</sub> in DMSO solvent. ClO<sub>4</sub><sup>-</sup> is also added to the simulations as the counter ion because LiClO<sub>4</sub> is believed as the most stable Li salt.<sup>34</sup> Figure 3a shows

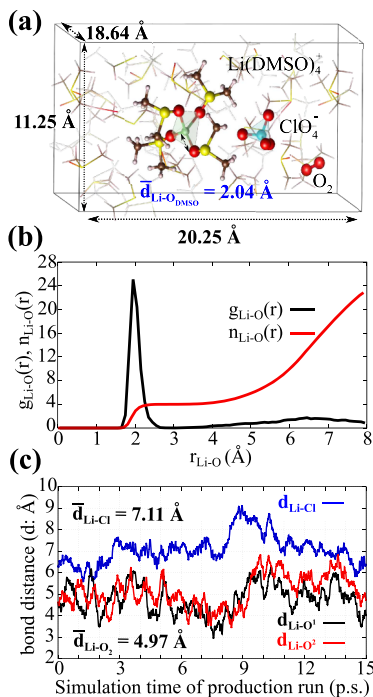


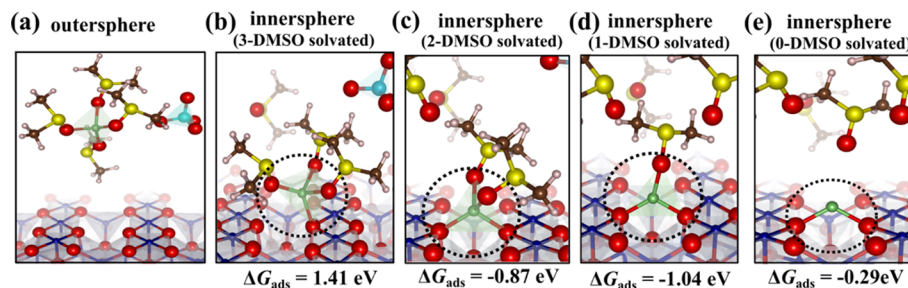
**Figure 3.** (a) Simulation box created for one pair of Li<sup>+</sup> and ClO<sub>4</sub><sup>-</sup> ions and the O<sub>2</sub> molecule in the explicit DMSO solvents. The equilibrated tetrahedral Li(DMSO)<sub>4</sub><sup>+</sup> structure is shown as the obtained stable first solvation shell, together with the averaged bond distance between Li<sup>+</sup> and O atoms (O from the four DMSO coordinates). (b) Partial Li–O radial distribution function [g<sub>Li–O(r)</sub>] and running coordination number [n<sub>Li–O(r)</sub>] for Li<sup>+</sup> in DMSO solvents. (c) Bond distance evolution of Li–Cl (from ClO<sub>4</sub><sup>-</sup>) and Li–O<sup>1</sup> and Li–O<sup>2</sup> (from O<sub>2</sub>) during the 15 ps AIMD production run in the explicit DMSO solvent.

a well-equilibrated first solvation shell of Li<sup>+</sup> in DMSO solvent from 25 ps *ab initio* molecular dynamics (AIMD) simulations (10 ps equilibration and 15 ps production run) and post-statistical analysis. The Li<sup>+</sup> component is observed in a stable

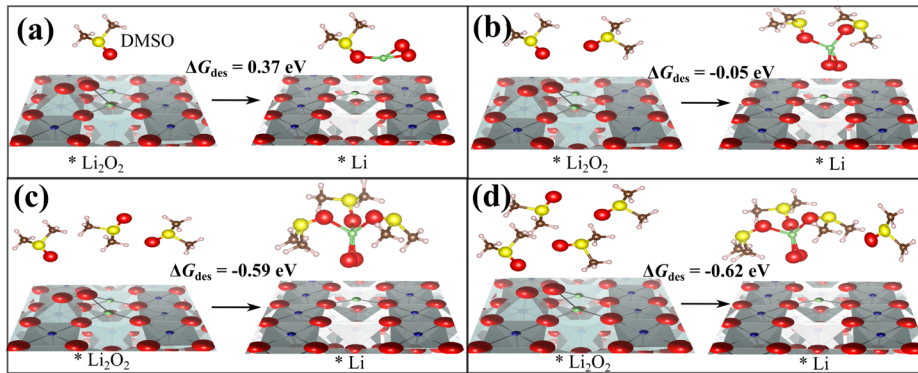
tetrahedral structure with four DMSO molecules as coordinates, where O atoms in DMSO act as the coordinating sites. The averaged distance of four Li–O bonds in the Li(DMSO)<sub>4</sub><sup>+</sup> solvation shell is 2.04 Å from a 15 ps production run. This well-defined tetrahedral Li(DMSO)<sub>4</sub><sup>+</sup> solvation structure also corresponds to the running coordination number (red line in Figure 3b) keeping at four in the  $d_{\text{Li}-\text{O}_{\text{DMSO}}}$  range from 2.0 to 4.0 Å. The distance evolution of Li<sup>+</sup>–O (from O<sub>2</sub>) and Li<sup>+</sup>–Cl (from ClO<sub>4</sub><sup>-</sup>) bonds is also plotted in Figure 3c. As shown, the  $d_{\text{Li}-\text{O}}$  mainly fluctuates above 4.0 Å (4.97 Å in average) and  $d_{\text{Li}-\text{Cl}}$  generally fluctuates above 6.0 Å (7.11 Å in average). All the above AIMD analyses confirm that the Li(DMSO)<sub>4</sub><sup>+</sup> configuration is the stable solvation shell for the Li<sup>+</sup> component in DMSO electrolyte, which is taken into the adsorption (desolvation) reaction simulations at the Co<sub>3</sub>O<sub>4</sub>(100)-O/DMSO (electrode/electrolyte) interface in the following paragraph.

Figure 4 shows a systematic comparison of the adsorption configurations for an explicit Li(DMSO)<sub>4</sub><sup>+</sup> solvation shell on the Co<sub>3</sub>O<sub>4</sub>(100)-O surface. Compared with the outer-sphere structure (Figure 4a),  $*\text{Li}(\text{DMSO})_3$  is thermodynamically unfavorable ( $\Delta G^0 = 1.41$  eV) to be adsorbed on the top site of the surface O atom (Figure 4b). All the other three inner-sphere adsorptions are found thermodynamically favorable, where Li atoms (coordinated with 0, 1, or 2 DMSO ligands) are located at the O–O bridge site of the Co<sub>3</sub>O<sub>4</sub>(100)-O surface. Among them, the  $*\text{Li}(\text{DMSO})$  adsorbate in Figure 4d is the most favorable configuration ( $\Delta G^0 = -1.04$  eV). Therefore, we confirmed that Li<sup>+</sup>/e<sup>-</sup> will be transferred to the surface O–O bridge site (without subsurface tetrahedral Co) of the Co<sub>3</sub>O<sub>4</sub>(100)-O surface as shown in Figure 2. Here, it is notable that although the effect of one DMSO ligand (binding to  $*\text{Li}$ ) is ignored when we calculate theoretical overpotentials in Figure 2, the derived overpotentials can still provide a reasonable prediction. The detailed explanation can be found in the above section of the thermodynamic overpotential study. After that, the DMSO ligand (in Figure 4d) can be released by the further O<sub>2</sub> adsorption on top of this  $*\text{Li}$  to form the final Li<sub>2</sub>O<sub>2</sub> products.

After the first Li<sub>2</sub>O<sub>2</sub> formed on the Co<sub>3</sub>O<sub>4</sub>(100)-O surface, we found that the partial LiO<sub>2</sub> monomer (in  $*\text{Li}_2\text{O}_2$  adsorbate) can be desorbed from the electrode surface to DMSO electrolyte. As shown in Figure 5, we considered the LiO<sub>2</sub> desorption reaction ( $\Delta G_{\text{des}} = G_{*\text{Li}} + G_{\text{LiO}_2(\text{DMSO})_n} - G_{*\text{Li}_2\text{O}_2} - n \times G_{\text{DMSO}}$ , where  $n = 1, 2, 3$ , and 4) assisted with  $n$  explicit DMSO molecules. We found that the desorption reaction is exothermic ( $\Delta G_{\text{des}} = -0.59$  eV) to form a three-coordinated



**Figure 4.** (a) Outer-sphere structure of the Li(DMSO)<sub>4</sub><sup>+</sup> solvation shell and ClO<sub>4</sub><sup>-</sup> on the Co<sub>3</sub>O<sub>4</sub>(100)-O surfaces. (b–e) Inner-sphere adsorption structures of Li(DMSO)<sub>n</sub><sup>+</sup> ( $n = 3, 2, 1$ , and 0) on the Co<sub>3</sub>O<sub>4</sub>(100)-O surfaces, together with their adsorption energies. ( $\Delta G_{\text{ads}} = G_{\text{inner-sphere}} - G_{\text{outer-sphere}}$ ).



**Figure 5.** (a–d) Desorption of the LiO<sub>2</sub> monomer from the Co<sub>3</sub>O<sub>4</sub>(100) surface to DMSO electrolyte with the assistance of one-four explicit DMSO molecules, respectively.

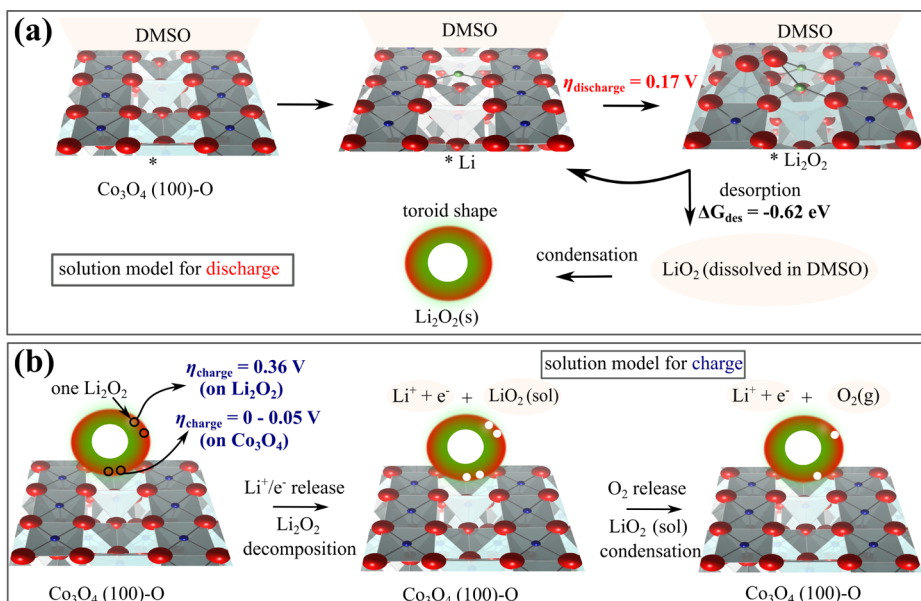
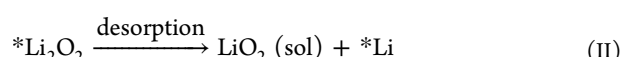
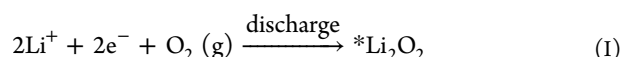


**Figure 6.** (a) Solution model pathway for discharge reactions on the Co<sub>3</sub>O<sub>4</sub>(100)-O surfaces. The  $\Delta G_{des}$  indicates the desorption free energy of the LiO<sub>2</sub> monomer from the Co<sub>3</sub>O<sub>4</sub>(100) surface to DMSO electrolyte shown in Figure 5. (b) Solution model pathway for charge reactions on the Co<sub>3</sub>O<sub>4</sub>(100)-O surfaces.

solvation structure, while the fourth explicit DMSO only slightly contributes to the LiO<sub>2</sub> desorption reaction because it will not enter into the first solvation shell of LiO<sub>2</sub>(DMSO)<sub>3</sub>. The three-coordinated solvation structure of LiO<sub>2</sub> has also been reported previously using AIMD simulations.<sup>42</sup> Therefore, we confirmed that the LiO<sub>2</sub> desorption reaction is favorable at the interface of the Co<sub>3</sub>O<sub>4</sub>(100)-O cathode and DMSO electrolyte, which provides a special solution model (see below discussion) for discharging/charging processes in the Li-air batteries.

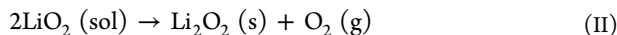
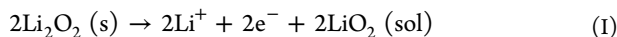
**Solution Model for Discharging/Charging Process at the Co<sub>3</sub>O<sub>4</sub>(100)-O Electrode and DMSO Electrolyte.** In the system of the Co<sub>3</sub>O<sub>4</sub>(100)-O electrode and DMSO electrolyte, the solution model is preferred because the desorption of LiO<sub>2</sub> is thermodynamically favorable from the cathode to the electrolyte. Therefore, in Figure 6a, the general mechanism and overpotential for Li–O<sub>2</sub> discharge reactions at the interface of the Co<sub>3</sub>O<sub>4</sub>(100)-O cathode and DMSO electrolyte is shown. The discharge pathways in such a system can be described in three main steps



Step I is to form a \*Li<sub>2</sub>O<sub>2</sub> monomer on the cathode, showing a discharge overpotential of  $\eta_{\text{discharge}} = 0.17 \text{ V}$  in Figure 2b. Then, step II is to desorb one LiO<sub>2</sub> molecule from the cathode surface to DMSO electrolyte. When the concentration of LiO<sub>2</sub>(sol) increases in the electrolyte, the sparingly soluble Li<sub>2</sub>O<sub>2</sub> will precipitate, contributing to growth of a toroidal particle (step III).<sup>32,33,43,44</sup> Furthermore, the active O–O bridge site on the Co<sub>3</sub>O<sub>4</sub>(100)-O surface becomes available for the next \*Li<sub>2</sub>O<sub>2</sub> formation (after LiO<sub>2</sub> desorbs in step II). As a result, the long-term surface discharge reaction will be  $*\text{Li} + \text{Li}^+ + \text{e}^- + \text{O}_2 \rightarrow *\text{Li}_2\text{O}_2$ , providing a constant  $\eta_{\text{discharge}} = 0.17 \text{ V}$  during the whole discharging process. Here, it is worth noting that the steps I and II of our mechanisms are slightly different from the steps of a and b (see the Introduction section) deduced from experiments. The reason

is that the formation of  $^*\text{Li}$  intermediates is more favorable than that of  $^*\text{LiO}_2$  intermediates on the  $\text{Co}_3\text{O}_4(100)\text{-O}$  surface (see the above mechanistic section). Therefore, the desorption of  $\text{LiO}_2$  only proceeds after the whole  $^*\text{Li}_2\text{O}_2$  monomer is formed on the  $\text{Co}_3\text{O}_4(100)\text{-O}$  surface.

Figure 6b shows the general solution model of the charge process [toroid  $\text{Li}_2\text{O}_2$  (s) decomposition] at the interface of DMSO/ $\text{Co}_3\text{O}_4(100)\text{-O}$ . We consider the decomposition from both the  $\text{Li}_2\text{O}_2$  surface and the  $\text{Co}_3\text{O}_4(100)\text{-O}$  surface. On the  $\text{Co}_3\text{O}_4(100)\text{-O}$  surface,  $\eta_{\text{charge}} = 0$  V for the pathway of  $^*\text{Li}_2\text{O}_2 \rightarrow ^*\text{Li} + \text{Li}^+ + \text{e}^- + \text{O}_2$  is obtained. Although this pathway provides a zero overpotential, the decomposition reaction is sluggish because almost whole of the  $\text{Li}_2\text{O}_2$  (s) particle surface area is neither resting on nor adjacent to the  $\text{Co}_3\text{O}_4(100)\text{-O}$  surface. To accelerate the decomposition (*i.e.*, make the charging process rapid), it is better to make the decomposition of  $\text{Li}_2\text{O}_2$  favorable from its own surface. According to previous studies,  $\eta_{\text{charge}} = 0.36$  V is required for the decomposition reaction on the  $\text{Li}_2\text{O}_2(0001)\text{-O}$ -rich surface.<sup>38</sup> Therefore, a reasonable overpotential of 0.36 V is required for the fast charging process in such a system, where the decomposition of  $\text{Li}_2\text{O}_2$  (s) will start from both toroid  $\text{Li}_2\text{O}_2$  and  $\text{Co}_3\text{O}_4(100)\text{-O}$  surfaces together. The decomposition pathways shown in Figure 6b can be summarized into the following two steps



Finally, it is worth noting that our calculated  $\eta_{\text{discharge}} = 0.17$  V (on the  $\text{Co}_3\text{O}_4(100)\text{-O}$  surface) is in good agreement with experimental  $\eta_{\text{discharge}} \approx 0.1\text{--}0.3$  V on  $\text{Co}_3\text{O}_4$  particles.<sup>16,20,45</sup> However, the predicted overpotential of 0.36 V for  $\text{Li}_2\text{O}_2$  (s) decomposition is much smaller than the reported  $\eta_{\text{charge}} \approx 1$  V in the experiment.<sup>16,20,45</sup> Moreover, according to previous experimental reports,  $\eta_{\text{charge}} > 1$  V was found on most of the other cathode materials in Li-air batteries,<sup>16</sup> although the  $\eta_{\text{charge}}$  demand is found in a range of 0.2–0.6 V for  $\text{Li}_2\text{O}_2$  decomposition (from all facets of the  $\text{Li}_2\text{O}_2$  crystal) even without any catalyst.<sup>38,40</sup> This theoretical and experimental  $\eta_{\text{charge}}$  discrepancy is due to the potential required to decompose the side product of lithium carbonate (including  $\text{Li}_2\text{CO}_3$ ) formed during discharge, which has been detected as the main side product of many transition metal oxides (including  $\text{Co}_3\text{O}_4$ ).<sup>45,46</sup> The decomposition voltage of lithium carbonate is about 4.0–4.5 V (*vs* RHE) in experiment,<sup>46,47</sup> which corresponds to  $\eta_{\text{charge}} \approx 1\text{--}1.5$  V in Li-air batteries. Therefore, in order to decrease the large  $\eta_{\text{charge}}$  (toward Li-air batteries) observed in realistic battery prototypes, it is more important to deal with the formation of the side product lithium carbonate rather than the decomposition of  $\text{Li}_2\text{O}_2$  on the  $\text{Co}_3\text{O}_4$  cathode.

## CONCLUSIONS

In this paper, a systematic first-principles thermodynamic study of Li-air batteries consisting of a  $\text{Co}_3\text{O}_4$  cathode and DMSO electrolyte is performed. We have investigated the surface structure, stable reconstructions, and the electronic properties of  $\text{Co}_3\text{O}_4$ . The  $\text{Co}_3\text{O}_4(100)\text{-O}$  surface is found to be the most stable one under standard conditions and all conditions in the bulk  $\text{Co}_3\text{O}_4$  stability region. The  $\text{Li}^+$  solvation structure in the DMSO-based electrolyte is determined as a tetrahedral  $\text{Li}(\text{DMSO})_4^+$  solvation shell from 25 ps AIMD equilibrations. Once a  $^*\text{Li}_2\text{O}_2$  discharge product is formed on the cathode

surface, the partial  $\text{LiO}_2$  monomer is found energetically favorable to be desorbed into the DMSO solvent, leaving empty active sites (on the cathode surface) for the next  $^*\text{Li}_2\text{O}_2$  product formation. As a result, in such a system of the  $\text{Co}_3\text{O}_4(100)\text{-O}$  surface and DMSO solvent, the discharge reactions follow a solution model with a constant  $\eta_{\text{discharge}} = 0.17$  V. Meanwhile, a 0.36 V overpotential is required to decompose  $\text{Li}_2\text{O}_2$  from its surface in order to obtain a rapid charging process. The higher  $\eta_{\text{charge}} \approx 1$  V observed in experiment is due to the voltage demand to decompose the side product lithium carbonate (including  $\text{Li}_2\text{CO}_3$ ) formed during discharge. Besides this, the kinetic barriers of the interface adsorption/desorption process also limit the overall efficiency of the Li-air batteries, which requires more studies in the future. In general, the present study shows that low  $\eta_{\text{discharge}}$  is achievable and understandable; avoiding the formation of side products on  $\text{Co}_3\text{O}_4$  in order to reduce  $\eta_{\text{charge}}$  is one of the main technical challenges on the road to efficient Li-air batteries.

## ASSOCIATED CONTENT

### Supporting Information

The Supporting Information is available free of charge at <https://pubs.acs.org/doi/10.1021/acs.jpcc.1c07619>.

Computational details; less energetically favorable mechanism for the  $\text{Li} + \text{O}_2$  reactions on the  $\text{Co}_3\text{O}_4(100)\text{-O}$  surface; and results and discussion of the  $\text{Li} + \text{O}_2$  reactions on the  $\text{Co}_3\text{O}_4(100)\text{-S}$  and  $(100)\text{-R}$  surfaces (PDF)

## AUTHOR INFORMATION

### Corresponding Author

Andrew M. Rappe – Department of Chemistry, University of Pennsylvania, Philadelphia, Pennsylvania 19104-6323, United States;  orcid.org/0000-0003-4620-6496; Email: rappe@sas.upenn.edu

### Author

Zhen Jiang – Department of Chemistry, University of Pennsylvania, Philadelphia, Pennsylvania 19104-6323, United States;  orcid.org/0000-0002-1175-5658

Complete contact information is available at: <https://pubs.acs.org/10.1021/acs.jpcc.1c07619>

### Notes

The authors declare no competing financial interest.

## ACKNOWLEDGMENTS

Z.J. and A.M.R. acknowledge support from the U.S. Department of Energy, Office of Science, Basic Energy Sciences, under award # DE-SC0019281. The authors thank Tian Qiu for help with the *ai*-GCMC calculations and Arvin Kakehni for meaningful discussions. Computational support was provided by the National Energy Research Scientific Computing Center (NERSC), a U.S. Department of Energy, Office of Science User Facility located at Lawrence Berkeley National Laboratory, operated under contract no. DE-AC02-05CH11231.

## REFERENCES

- Goodenough, J. B.; Park, K.-S. The Li-ion rechargeable battery: a perspective. *J. Am. Chem. Soc.* 2013, 135, 1167–1176.

- (2) Bonaccorso, F.; Colombo, L.; Yu, G.; Stoller, M.; Tozzini, V.; Ferrari, A. C.; Ruoff, R. S.; Pellegrini, V. 2D materials. Graphene, related two-dimensional crystals, and hybrid systems for energy conversion and storage. *Science* **2015**, *347*, 1246501.
- (3) Li, M.; Qiu, T.; Foucher, A. C.; Fu, J.; Wang, Z.; Zhang, D.; Rappe, A. M.; Stach, E. A.; Detsi, E. Impact of Hierarchical Nanoporous Architectures on Sodium Storage in Antimony-Based Sodium-Ion Battery Anodes. *ACS Appl. Energy Mater.* **2020**, *3*, 11231–11241.
- (4) Jiang, Z.; Alexandrov, V. Electrocatalytic activity of oxygen-functionalized carbon electrodes for vanadium redox flow batteries from free-energy calculations. *ACS Appl. Energy Mater.* **2020**, *3*, 7543–7549.
- (5) Xu, Y.; Shelton, W. A. O<sub>2</sub> reduction by lithium on Au (111) and Pt (111). *J. Chem. Phys.* **2010**, *133*, 024703.
- (6) Li, X.; Gu, M.; Hu, S.; Kennard, R.; Yan, P.; Chen, X.; Wang, C.; Sailor, M. J.; Zhang, J.-G.; Liu, J. Mesoporous silicon sponge as an anti-pulverization structure for high-performance lithium-ion battery anodes. *Nat. Commun.* **2014**, *5*, 4105.
- (7) Intan, N. N.; Klyukin, K.; Alexandrov, V. Ab initio modeling of transition metal dissolution from the LiNi<sub>0.5</sub>Mn<sub>1.5</sub>O<sub>4</sub> cathode. *ACS Appl. Mater. Interfaces* **2019**, *11*, 20110–20116.
- (8) Luntz, A. C.; McCloskey, B. D. Nonaqueous Li-air batteries: a status report. *Chem. Rev.* **2014**, *114*, 11721–11750.
- (9) Lim, H.-D.; Lee, B.; Bae, Y.; Park, H.; Ko, Y.; Kim, H.; Kim, J.; Kang, K. Reaction chemistry in rechargeable Li-O<sub>2</sub> batteries. *Chem. Soc. Rev.* **2017**, *46*, 2873–2888.
- (10) Kondori, A.; et al. Kinetically Stable Oxide Overlayers on Mo<sub>3</sub>P Nanoparticles Enabling Lithium-Air Batteries with Low Overpotentials and Long Cycle Life. *Adv. Mater.* **2020**, *32*, 2004028.
- (11) Zhang, X.; Chen, A.; Jiao, M.; Xie, Z.; Zhou, Z. Understanding Rechargeable Li-O<sub>2</sub> Batteries via First-Principles Computations. *Batteries Supercaps* **2019**, *2*, 498–508.
- (12) Zhang, P.; Zhao, Y.; Zhang, X. Functional and stability orientation synthesis of materials and structures in aprotic Li-O<sub>2</sub> batteries. *Chem. Soc. Rev.* **2018**, *47*, 2921–3004.
- (13) Aurbach, D.; McCloskey, B. D.; Nazar, L. F.; Bruce, P. G. Advances in understanding mechanisms underpinning lithium-air batteries. *Nat. Energy* **2016**, *1*, 16128.
- (14) Tamakloe, W.; Agyeman, D. A.; Park, M.; Yang, J.; Kang, Y.-M. Polydopamine-induced surface functionalization of carbon nanofibers for Pd deposition enabling enhanced catalytic activity for the oxygen reduction and evolution reactions. *J. Mater. Chem. A* **2019**, *7*, 7396–7405.
- (15) Wang, C.; Xie, Z.; Zhou, Z. Lithium-air batteries: Challenges coexist with opportunities. *APL Mater.* **2019**, *7*, 040701.
- (16) Surya, K.; Michael, M. S.; Prabaharan, S. R. S. A review on advancement in non-noble metal based oxides as bifunctional catalysts for rechargeable non-aqueous Li/air battery. *Solid State Ionics* **2018**, *317*, 89–96.
- (17) Wang, J.; Gao, R.; Zhou, D.; Chen, Z.; Wu, Z.; Schumacher, G.; Hu, Z.; Liu, X. Boosting the electrocatalytic activity of Co<sub>3</sub>O<sub>4</sub> nanosheets for a Li-O<sub>2</sub> battery through modulating inner oxygen vacancy and exterior Co<sup>3+</sup>/Co<sup>2+</sup> ratio. *ACS Catal.* **2017**, *7*, 6533–6541.
- (18) Gao, R.; Yang, Z.; Zheng, L.; Gu, L.; Liu, L.; Lee, Y.; Hu, Z.; Liu, X. Enhancing the catalytic activity of Co<sub>3</sub>O<sub>4</sub> for Li-O<sub>2</sub> batteries through the synergy of surface/interface/doping engineering. *ACS Catal.* **2018**, *8*, 1955–1963.
- (19) Gao, R.; Shang, Z.; Zheng, L.; Wang, J.; Sun, L.; Hu, Z.; Liu, X. Enhancing the Catalytic Activity of Co<sub>3</sub>O<sub>4</sub> Nanosheets for Li-O<sub>2</sub> Batteries by the Incorporation of Oxygen Vacancy with Hydrazine Hydrate Reduction. *Inorg. Chem.* **2019**, *58*, 4989–4996.
- (20) Cui, Y.; Wen, Z.; Sun, S.; Lu, Y.; Jin, J. Mesoporous Co<sub>3</sub>O<sub>4</sub> with different porosities as catalysts for the lithium–oxygen cell. *Solid State Ionics* **2012**, *225*, 598–603.
- (21) Xiao, Z.; et al. Operando identification of the dynamic behavior of oxygen vacancy-rich Co<sub>3</sub>O<sub>4</sub> for oxygen evolution reaction. *J. Am. Chem. Soc.* **2020**, *142*, 12087–12095.
- (22) Zasada, F.; Piskorz, W.; Sojka, Z. Cobalt spinel at various redox conditions: DFT + U investigations into the structure and surface thermodynamics of the (100) facet. *J. Phys. Chem. C* **2015**, *119*, 19180–19191.
- (23) Xu, X.-L.; Chen, Z.-H.; Li, Y.; Chen, W.-K.; Li, J.-Q. Bulk and surface properties of spinel Co<sub>3</sub>O<sub>4</sub> by density functional calculations. *Surf. Sci.* **2009**, *603*, 653–658.
- (24) Shojaee, K.; Montoya, A.; Haynes, B. S. Insight into oxygen stability and vacancy formation on Co<sub>3</sub>O<sub>4</sub> model slabs. *Comput. Mater. Sci.* **2013**, *72*, 15–25.
- (25) Montoya, A.; Haynes, B. S. Periodic density functional study of Co<sub>3</sub>O<sub>4</sub> surfaces. *Chem. Phys. Lett.* **2011**, *502*, 63–68.
- (26) Lyu, Z.; et al. Effect of oxygen adsorbability on the control of Li<sub>2</sub>O<sub>2</sub> growth in Li-O<sub>2</sub> batteries: Implications for cathode catalyst design. *Nano Energy* **2017**, *36*, 68–75.
- (27) Dathar, G. K. P.; Shelton, W. A.; Xu, Y. Trends in the catalytic activity of transition metals for the oxygen reduction reaction by lithium. *J. Phys. Chem. Lett.* **2012**, *3*, 891–895.
- (28) Novčić, K. A.; Dobrota, A. S.; Petković, M.; Johansson, B.; Skorodumova, N. V.; Mentus, S. V.; Pašti, I. A. Theoretical analysis of doped graphene as cathode catalyst in Li-O<sub>2</sub> and Na-O<sub>2</sub> batteries—the impact of the computational scheme. *Electrochim. Acta* **2020**, *354*, 136735.
- (29) Jing, Y.; Zhou, Z. Computational insights into oxygen reduction reaction and initial Li<sub>2</sub>O<sub>2</sub> nucleation on pristine and N-doped graphene in Li-O<sub>2</sub> batteries. *ACS Catal.* **2015**, *5*, 4309–4317.
- (30) Ganapathy, S.; Adams, B. D.; Stenou, G.; Anastasaki, M. S.; Goubitz, K.; Miao, X.-F.; Nazar, L. F.; Wagemaker, M. Nature of Li<sub>2</sub>O<sub>2</sub> oxidation in a Li-O<sub>2</sub> battery revealed by operando X-ray diffraction. *J. Am. Chem. Soc.* **2014**, *136*, 16335–16344.
- (31) Liu, C.; Brant, W. R.; Younesi, R.; Dong, Y.; Edström, K.; Gustafsson, T.; Zhu, J. Towards an Understanding of Li<sub>2</sub>O<sub>2</sub> Evolution in Li-O<sub>2</sub> Batteries: An In Operando Synchrotron X-ray Diffraction Study. *ChemSusChem* **2017**, *10*, 1592–1599.
- (32) Lyu, Z.; Zhou, Y.; Dai, W.; Cui, X.; Lai, M.; Wang, L.; Huo, F.; Huang, W.; Hu, Z.; Chen, W. Recent advances in understanding of the mechanism and control of Li<sub>2</sub>O<sub>2</sub> formation in aprotic Li-O<sub>2</sub> batteries. *Chem. Soc. Rev.* **2017**, *46*, 6046–6072.
- (33) Johnson, L.; Li, C.; Liu, Z.; Chen, Y.; Freunberger, S. A.; Ashok, P. C.; Praveen, B. B.; Dholakia, K.; Tarascon, J.-M.; Bruce, P. G. The role of LiO<sub>2</sub> solubility in O<sub>2</sub> reduction in aprotic solvents and its consequences for Li-O<sub>2</sub> batteries. *Nat. Chem.* **2014**, *6*, 1091–1099.
- (34) Lai, J.; Xing, Y.; Chen, N.; Li, L.; Wu, F.; Chen, R. Electrolytes for Rechargeable Lithium-Air Batteries. *Angew. Chem., Int. Ed.* **2020**, *59*, 2974–2997.
- (35) Wexler, R. B.; Qiu, T.; Rappe, A. M. Automatic Prediction of Surface Phase Diagrams Using Ab Initio Grand Canonical Monte Carlo. *J. Phys. Chem. C* **2019**, *123*, 2321–2328.
- (36) Wang, L.; Maxisch, T.; Ceder, G. Oxidation energies of transition metal oxides within the GGA + U framework. *Phys. Rev. B: Condens. Matter Mater. Phys.* **2006**, *73*, 195107.
- (37) Walsh, A.; Wei, S.-H.; Yan, Y.; Al-Jassim, M. M.; Turner, J. A.; Woodhouse, M.; Parkinson, B. A. Structural, magnetic, and electronic properties of the Co-Fe-Al oxide spinel system: Density-functional theory calculations. *Phys. Rev. B: Condens. Matter Mater. Phys.* **2007**, *76*, 165119.
- (38) Hummelshøj, J.; Luntz, A.; Nørskov, J. Theoretical evidence for low kinetic overpotentials in Li-O<sub>2</sub> electrochemistry. *J. Chem. Phys.* **2013**, *138*, 034703.
- (39) Viswanathan, V.; Thygesen, K. S.; Hummelshøj, J. S.; Nørskov, J. K.; Girishkumar, G.; McCloskey, B. D.; Luntz, A. C. Electrical conductivity in Li<sub>2</sub>O<sub>2</sub> and its role in determining capacity limitations in non-aqueous Li-O<sub>2</sub> batteries. *J. Chem. Phys.* **2011**, *135*, 214704.
- (40) Mo, Y.; Ong, S. P.; Ceder, G. First-principles study of the oxygen evolution reaction of lithium peroxide in the lithium-air battery. *Phys. Rev. B: Condens. Matter Mater. Phys.* **2011**, *84*, 205446.
- (41) Li, X.; Li, Z.; Yang, X.; Jia, L.; Fu, Y. Q.; Chi, B.; Pu, J.; Li, J. First-principles study of the initial oxygen reduction reaction on

stoichiometric and reduced CeO<sub>2</sub> (111) surfaces as a cathode catalyst for lithium–oxygen batteries. *J. Mater. Chem. A* **2017**, *5*, 3320–3329.

(42) Scheers, J.; Lidberg, D.; Sodeyama, K.; Futera, Z.; Tateyama, Y. Life of superoxide in aprotic Li–O<sub>2</sub> battery electrolytes: simulated solvent and counter-ion effects. *Phys. Chem. Chem. Phys.* **2016**, *18*, 9961–9968.

(43) Zeng, J.; Francia, C.; Amici, J.; Bodoardo, S.; Penazzi, N. A highly reversible Li–O<sub>2</sub> battery utilizing a mixed electrolyte and a cathode incorporating Co<sub>3</sub>O<sub>4</sub>. *RSC Adv.* **2015**, *5*, 83056–83064.

(44) Aetukuri, N. B.; McCloskey, B. D.; García, J. M.; Krupp, L. E.; Viswanathan, V.; Luntz, A. C. Solvating additives drive solution-mediated electrochemistry and enhance toroid growth in non-aqueous Li–O<sub>2</sub> batteries. *Nat. Chem.* **2015**, *7*, 50–56.

(45) Lim, H.-D.; Gwon, H.; Kim, H.; Kim, S.-W.; Yoon, T.; Choi, J. W.; Oh, S. M.; Kang, K. Mechanism of Co<sub>3</sub>O<sub>4</sub>/graphene catalytic activity in Li–O<sub>2</sub> batteries using carbonate based electrolytes. *Electrochim. Acta* **2013**, *90*, 63–70.

(46) Balaish, M.; Jung, J. W.; Kim, I. D.; Ein-Eli, Y. A Critical Review on Functionalization of Air-Cathodes for Nonaqueous Li–O<sub>2</sub> Batteries. *Adv. Funct. Mater.* **2020**, *30*, 1808303.

(47) Seong, W. M.; Cho, K.-H.; Park, J.-W.; Park, H.; Eum, D.; Lee, M. H.; Kim, I.-s. S.; Lim, J.; Kang, K. Controlling Residual Lithium in High-Nickel (>90 %) Lithium Layered Oxides for Cathodes in Lithium-Ion Batteries. *Angew. Chem., Int. Ed.* **2020**, *59*, 18662–18669.